Longitudinal compression and Poisson ratio of fiber yarns in meso-scale finite element modeling of composite reinforcements

D. Wang, N. Naouar, E. Vidal-Salle, P. Boisse

Longitudinal compression and Poisson ratio of fiber yarns in meso-scale finite element modeling of composite reinforcements

D. Wang, N. Naouar, E. Vidal-Salle, P. Boisse*
Université de Lyon, LaMCoS, INSA-Lyon, F-69621, Villeurbanne, France

Abstract

Meso-scale finite element modeling is a powerful tool to analyze the deformation of textile composite reinforcements. At the meso-scale, the yarns of the reinforcement are considered to be solids made of a continuous material in contact with their neighbors. These yarns are generally under tension, but some loadings of the reinforcement lead to a longitudinal compression state. The yarns, made up of a large number of fibers, present a specific behavior when under longitudinal compression. Local buckling of the fibers causes the compressive stiffness of the continuous material representing the yarn to be much weaker than when under tension. In addition, longitudinal compression causes an important transverse expansion. It is shown in the present work that the transverse expansion could be depicted by a Poisson ratio that remained roughly constant when the yarn length and the compression strain varied. Buckling of the fibers significantly increases the transverse dimensions of the yarn which leads to a large Poisson ratio (up to 12 for a yarn analyzed in the present study). The longitudinal compression and transverse expansion were integrated in a mechanical model of the yarn. Meso-scale finite element simulations of reinforcements with binder yarns submitted to longitudinal compression showed that these improvements led to results in good agreement with micro-CT analyses.

Keywords: A. Fabrics/textiles; A. Preform; B. Mechanical properties;
C. Finite element analysis (FEA); Longitudinal compression

1. Introduction

Textile composite reinforcements, like the ones considered in this study, consist of weaved (or alternatively braided or stitched) yarns (Fig. 1). The yarns themselves are composed of a large number of continuous fibers, (e.g., 3000 to 48000 fibers in the case of a carbon fiber yarn). One can thus distinguish between the macroscopic scale (the scale of the preform) (Fig. 1a), the mesoscopic scale (the scale of the yarn) (Fig. 1b) and the microscopic scale (the scale of the fiber) (Fig. 1c) [1]. The

* Corresponding author. INSA avenue Jean Capelle, 69631 Villeurbanne, France.

simulation of the deformation of textile reinforcements during the so-called draping phase makes it possible to design the forming process but also to know the geometry of the reinforcement during the injection phase of Liquid Composite Molding (LCM) processes.

The three scales, i.e., macro, meso and micro, are simultaneously present in the composite reinforcements but numerical simulations are carried out at one of these scales (sometimes several). Many analyses are carried out at the macroscopic scale, particularly when simulating the shaping of the reinforcement [2-7] and the injection in LCM processes [8,9]. Simulations at lower scales on the other hand give information concerning the internal structure of the deformed fibrous reinforcement. Some simulations are carried out at the microscopic scale, i.e., by modeling all fibers and their contacts [10-13]. The fibers in a yarn, and consequently in a reinforcement, are numerous and these approaches only concern a small domain. Meso-scale finite element (FE) modeling of textile reinforcements considers the preform as a set of yarns in contact with their neighbors. These yarns are seen as continuous materials. Some simulations at the mesoscopic scale concern the complete preform, but most are carried out on periodic reinforcements and concern the Representative Unit Cell (RUC) (Fig. 1b1 in the case of a glass plain weave). This RUC is the smallest elementary pattern making it possible to obtain the entire reinforcement by translation [14].

Among many applications, mesoscopic analyses are used to determine homogenized properties [1, 14-18], damage initiation and development [1, 19-21]. Mesoscopic simulations of the RUC deformation during forming make it possible to determine the internal geometry of the yarns constituting the deformed reinforcement [22, 23]. This geometry conditions the permeability of the deformed reinforcement during injection [24-29]. The geometry of the yarns after forming also influences the mechanical properties of the final composite.

In most mesoscopic analyses of composite textile reinforcements, the yarns are under tension. This corresponds to the classical condition of putting the fiber yarns under stress or loading. Nevertheless, considering the internal geometry of the reinforcement and the interlaces due to weaving, some yarns may be in a state of compression in the direction of the fibers (longitudinal compression). This is particularly the case during the compaction phase of a reinforcement that precedes the injection phase in an LCM process. If the reinforcement has binder yarns or yarns through the thickness (z-yarns), these can be in longitudinal compression. Experimental analysis and

simulation of the behavior of composite reinforcement yarns in longitudinal compression is the topic of this article.

Two main aspects are addressed. The stiffness in longitudinal compression of a fiber yarn (such as those used for composite reinforcements) is much smaller than the stiffness of this yarn under tension. The longitudinal compression behavior is analyzed experimentally and then integrated into the constitutive model used for the mesoscopic simulations of the deformation of the RUC. The second point analyzed is the transverse expansion during longitudinal compression of a fiber yarn. This expansion is important given the individual buckling of the fibers during longitudinal compression. The individual fibers buckle but the yarn, seen as a continuous material at the mesoscopic scale, expands by the Poisson effect.

Some studies have been carried out to determine the Poisson ratio of fiber yarns. They concern the transverse strains of yarns under tension [30-34]. Some of these investigations have dealt with auxetic yarns, i.e., yarns with negative Poisson ratios [31-33]. However, to the best of our knowledge, there are no analyses of the transverse expansion of yarn in longitudinal compression, and this is thus one of the main goals of the present paper. It was shown by experiments that the ratio between the transverse expansion and the longitudinal compression was relatively constant for different compression ratios and various yarn dimensions. Consequently, one can propose a Poisson ratio which defines the transverse expansion of the yarn. The value of this ratio can be substantial (e.g., 11 for the analyzed reinforcement).

The constitutive law taking into account the measured longitudinal compression and transverse expansion was used for the mesoscopic simulations of the compaction of the RUC of two composite reinforcements. The deformation of the yarns in longitudinal compression obtained by these simulations was found to be in good agreement with the experimental deformation achieved by X-ray tomography.

2. Meso-scale finite element (FE) modeling of textile composites

2.1. A mesoscopic mechanical model for fiber yarns

During analysis at the mesoscopic scale, the fiber yarn is seen as an anisotropic continuous material. The yarns that were considered in this study were assumed to be a set of parallel fibers as

shown in Fig. 2. The twist of the fiber was neglected which was justified for a small twist angle and if the segment of yarn was sufficiently short. Meso-FE modeling of the yarn requires a constitutive law that conveys the specific fibrous nature of the yarns that are assumed to be continuous solids, made of fibers, in a single direction. Among continuous mechanical models at large strain, rate constitutive equations are widely used [35-37] to relate the stress and strain rates:

$$\underline{\underline{\sigma}}^{\nabla} = \underline{\underline{\underline{\underline{C}}}} : \underline{\underline{D}} \tag{1}$$

Here, $\underline{\underline{D}}$ is the strain rate tensor, $\underline{\underline{\underline{\underline{C}}}}$ is the constitutive tensor and $\underline{\underline{\sigma}}^{\nabla}$ is an objective time derivative of the Cauchy stress $\underline{\underline{\sigma}}$. The objective stress rate $\underline{\underline{\sigma}}^{\nabla}$ is the time derivative for an observer fixed with respect to the material. It avoids the stress change due to the rigid body rotation that exists in $\dot{\underline{\underline{\sigma}}} = \frac{d\underline{\underline{\sigma}}}{dt}$. The objective derivative can be defined from the rotation $\underline{\underline{Q}}$ of the rotated frame:

$$\underline{\underline{\sigma}}^{\nabla} = \dot{\underline{\underline{\sigma}}} - \underline{\underline{\Omega}} \cdot \underline{\underline{\sigma}} + \underline{\underline{\sigma}} \cdot \underline{\underline{\Omega}} = \underline{\underline{Q}} \left(\frac{d}{dt} \left(\underline{\underline{Q}}^{T} \cdot \underline{\underline{\sigma}} \cdot \underline{\underline{Q}} \right) \right) \cdot \underline{\underline{Q}}^{T} \tag{2}$$

where $\underline{\underline{\Omega}} = \dot{\underline{\underline{Q}}} \cdot \underline{\underline{Q}}^{T}$ is the rotation rate. The "rotated frame" rotates with the material. It is not unique. The most used rotations include that of the polar decomposition of the deformation gradient (Green-Naghdi objective derivative) [38, 39] or the co-rotational frame rotation (Jaumann objective derivative) [40, 41]. They express the mean rotation of isotropic materials such as metals. Neither of them is suitable for fibrous materials, because the behavior of the fibrous medium is highly related to the fiber orientation which should be strictly followed [42, 43]. In the case of a fibrous material with a single direction of fibers, the rotation $\underline{\underline{\Phi}}$ must be that of the fiber [22, 42, 43]. The rotated basis is attached to the fiber direction $\underline{f}_1$. The second basis vector $\underline{f}_2$ is the projection of its materially convected initial position into the plane perpendicular to the fiber direction $\underline{f}_1$. Finally $\underline{f}_3$ is orthogonal to $\underline{f}_1$ and $\underline{f}_2$.

In a simulation of the deformation of a reinforcement at mesoscopic state, Eq. (1) is integrated using the Hughes-Winget scheme over $\Delta t = t^{n+1} - t^{n}$ [44]:

$$\left[\sigma^{n+1} \right]_{f_i^{n+1}} = \left[\sigma^{n} \right]_{f_i^{n}} + \left[\mathrm{C}^{n+1/2} \right]_{f_i^{n+1/2}} \left[\Delta\varepsilon^{n+1} \right]_{f_i^{n+1/2}} \tag{3}$$

The analysis requires the components of the constitutive matrix [C] in the frame $\underline{f}_i$.

Fig. 3 shows the different deformation modes of the fiber yarn. Although longitudinal compression was the goal of this paper, this section first considers, in order to present pre-existent models, the case of yarns under tension, which is the most common case [45]. In section 3 and those following, the case of compression in the direction of the fibers (longitudinal compression), which is the main objective of this study, is analyzed.

The longitudinal Young modulus E_l (Fig. 3a) was measured by a tensile experiment on the single yarn. The yarn could be considered transversely isotropic [22], and consequently it had a single longitudinal shear coefficient G_{lt}. This coefficient is small because of possible slippage between fibers in the yarn. It was identified by an inverse approach in a tensile test on a woven fabric. The mechanical behavior in the transverse section was defined by the surface change (Fig. 3b) and the transverse section shear (Fig. 3c). Consequently, the strain field in the yarn's cross section $[\varepsilon_t]_f$ can be decomposed into a spherical part and a deviatoric part [22]:

$$[\varepsilon_t]_f = \begin{bmatrix} \varepsilon_s & 0 \\ 0 & \varepsilon_s \end{bmatrix} + \begin{bmatrix} \varepsilon_d & \varepsilon_{23} \\ \varepsilon_{23} & -\varepsilon_d \end{bmatrix} \tag{4}$$

Here, ε_s is the spherical strain component ($\varepsilon_s = (\varepsilon_{22} + \varepsilon_{33})/2$), and ε_d and ε_{23} are the deviatoric strain components ($\varepsilon_d = (\varepsilon_{22} - \varepsilon_{33})/2$). The decomposition holds for transverse strain and stress increments $[\Delta\varepsilon_t]_f$ and $[\Delta\sigma_t]_f$, which leads to the following constitutive relations:

$$\Delta\sigma_s = A\Delta\varepsilon_s \qquad \Delta\sigma_d = B\Delta\varepsilon_d \qquad \Delta\sigma_{23} = C\Delta\varepsilon_{23} \tag{5}$$

where A, B and C are stiffness parameters. *B* and *C* are equal because of the isotropy in the transverse section of the yarn, and A provides the resistance to the variation of sectional area. *A* and *B* depend on the strain in the yarn. The following forms have be proposed and identified [22]:

$$A = A_0 e^{-p\varepsilon_s} e^{n\varepsilon_l} \qquad B = B_0 e^{-p\varepsilon_s} \tag{6}$$

The unknown parameters (A_0, B_0, p, n) can be identified by transverse compaction and biaxial tension experiments with the Levenberg-Marquardt inverse fitting algorithm [46]. In case of tension to the yarn, the change in transverse section is small, in particular for a yarn made of parallel fibers, and the Poisson ratio can be set to zero. Finally, the constitutive matrix $[C]_f$ of Eq. (3) is expressed as:

$$[C]_f = \begin{bmatrix} E_l & 0 & 0 & 0 & 0 & 0 \\ & \frac{A+B}{2} & \frac{A-B}{2} & 0 & 0 & 0 \\ & & \frac{A+B}{2} & 0 & 0 & 0 \\ & & & G_{lt} & 0 & 0 \\ & sym. & & & B & 0 \\ & & & & & G_{lt} \end{bmatrix} \quad (7)$$

This mesoscopic mechanical model has been applied to simulate different modes of deformation of textile composite reinforcements and proved to be effective [22, 42, 47].

A very unbalanced textile composite reinforcement is presented in Fig. 4. It is composed of three kinds of glass fiber yarns: warp yarns, weft yarns and binder yarns, where the warp yarn was much larger than the other two. The tensile stiffness of the yarns and the transverse mechanical parameters are given in Table 1.

It should be emphasized that the constitutive relation proposed above corresponds to cases where the yarns are under tension. The tensile modulus represents the tension stiffness. The compression stiffness in the fiber direction is different because of the fibrous constitution of the yarn. In addition, the Poisson ratios are assumed to be equal to zero. This assumption is possible for a yarn made of parallel fibers under tension as each fiber tends to be straight (Fig. 2). When a yarn is in longitudinal compression, on the other hand, there are induced transverse displacements.

The next section demonstrates that the form of the constitutive matrix given in Eq. (7) is not sufficient to simulate the compaction of the textile reinforcement presented in section 2.2 due to the longitudinal compression of the binder yarn. Sections 3 through 5 analyze and introduce the longitudinal compression stiffness and the corresponding transverse expansion in the constitutive model.

2.2. Simulation of the compaction of the textile reinforcement

A transverse compaction of the textile reinforcement, shown in Fig. 4, was carried out inside an X-ray computed tomography system (Fig. 5). The textile reinforcement was compacted between two Plexiglas plates according to the following: initial thickness= 0.72 mm, thickness after compaction = 0.40 mm, $\varepsilon_{compaction}$ = 44%. The micro-CT analysis gave the experimental deformed geometry of the yarns of the fabric after compaction (Fig. 6). The Plexiglas plates are not removed. They prescribed

the compaction deformation and they do not modify the scanning quality. The simulation of this global compaction was carried out using the mesh of the RUC, as shown in Fig. 7. The mesh was obtained from the X-ray tomography analysis [47, 48]. Periodic boundary conditions are used for the Representative Unit Cell (RUC) [14, 43]. Two points of the boundary in so-called paired positions on two opposite boundaries have the same displacements.

The deformed shape obtained by simulation (using the constitutive model presented in section 2.1) is shown in Fig. 8. The simulated shape of the binder yarn was not correct. It presented wrinkles that were not observed in the micro-CT analysis. In addition, the width of the deformed binder yarn was smaller than the experimental one (Fig. 6 and 8). This binder yarn was subjected to longitudinal compression (Fig. 8) which could not be correctly modeled by the constitutive law presented above. In the following sections, the longitudinal compaction behavior and the related transverse expansion are analyzed and taken into account in the constitutive model.

3. Longitudinal compression of the fiber yarn

The longitudinal compression stiffness K_l^{comp} ($K_l^{comp} = S_l E_l^{comp}$) of the binder yarns was measured by longitudinal compression experiments. The experimental setup and the tested specimens are shown in Fig. 9. The resistance of the yarns to longitudinal compression was small, and consequently a high accuracy force sensor was required (the one in this study was a 10-N sensor). Moreover, it was advised to compress several yarns at the same time (Fig. 9b). The compression velocity was 2 mm/min, which was slow enough to eliminate the dynamic influence.

The longitudinal compression stiffness curves of the binder yarn are presented in Fig. 9c. The compression behavior of the yarn was almost linear in the first part of the curve after which the yarn buckled and the stiffness decreased. The buckling occurred sooner when the yarn was longer. Nevertheless, it was assumed that, during the analyzed reinforcement deformation the length of the yarns and the boundary conditions are such that there is no global buckling of the yarns and that the longitudinal compression stiffness was given by the first linear part of the test presented in Fig 9c.

It should be noted that the longitudinal compression stiffness before buckling did not depend on the length of the yarn (or very little). The longitudinal compression stiffness of the binder yarn tested in Fig. 9 was $K_l^{comp} = 2.1\,N$ which was much lower than the longitudinal tension stiffness. This

was taken into account in the constitutive matrix Eq. (7) in the case of longitudinal compression. In practice, the large difference between the longitudinal tension and compression stiffnesses can lead to numerical difficulties in the transition zone. These problems were avoided by a smoothing of the tension-strain curve. In Fig. 10, when the longitudinal strains $\varepsilon_l^n, \varepsilon_l^{n+1}$ at the beginning and at the end of the step were such that $\varepsilon_l^{n+1}\varepsilon_l^n < 0$ (i.e., among the longitudinal strains at the beginning and at the end of the step, one was under tension and one was in compression), the longitudinal stiffness of the yarn used to update the tension stress at t^{n+1} was:

$$K_l = \frac{K_l(\varepsilon_l^{n+1})\,\varepsilon_l^{n+1} - K_l(\varepsilon_l^n)\,\varepsilon_l^n}{\varepsilon_l^{n+1} - \varepsilon_l^n} \tag{8}$$

4. Transverse expansion. Poisson ratio in longitudinal compression.

The initial shape of the constitutive matrix Eq. (7) neglects the transverse expansions. This is fairly well justified if the yarn is under tension and when it consists of parallel fibers such as those of the yarns shown in Fig.2 and 4. When the yarn is in longitudinal compression, the cross-section of the yarn increases significantly (Fig. 11c). It is thus necessary to take into account this transversal expansion in the mechanical behavior. For this, a Poisson ratio ν_{lt} is introduced into the constitutive matrix.

$$[D] = [C]^{-1} = \begin{bmatrix} \frac{1}{E_l} & -\frac{\nu_{lt}}{E_l} & -\frac{\nu_{lt}}{E_l} & 0 & 0 & 0 \\ & \frac{A+B}{2A\cdot B} & \frac{B-A}{2A\cdot B} & 0 & 0 & 0 \\ & & \frac{A+B}{2A\cdot B} & 0 & 0 & 0 \\ & & & \frac{1}{G_{lt}} & 0 & 0 \\ & sym & & & \frac{1}{B} & 0 \\ & & & & & \frac{1}{G_{lt}} \end{bmatrix} \qquad [C] = [D]^{-1} \begin{bmatrix} E_t & \nu_{lt}A & \nu_{lt}A & 0 & 0 & 0 \\ & \frac{A+B}{2} & \frac{A-B}{2} & 0 & 0 & 0 \\ & & \frac{A+B}{2} & 0 & 0 & 0 \\ & & & G_{lt} & 0 & 0 \\ & & & & B & 0 \\ & & & & & G_{lt} \end{bmatrix} \tag{9}$$

The mechanical behavior of the yarn in the transverse plane has been proven to be isotropic [22]. To analyze the transverse expansion, an experimental analysis of the geometry of the fiber yarn in longitudinal compaction was carried out. Fig. 11 shows the compression system and the camera that records the longitudinal compression and the transverse expansion (Fig.11c). A lamp improved the contrast between the yarn and the background (Fig 11b). The lengths of the tested samples were of the

same order as those of the yarns in the woven reinforcement and were in the range 5 to 10 mm. Fig. 12 shows the transverse expansion obtained experimentally in the case of the binder yarn (of the fabric shown in Fig. 4) for a longitudinal compression of 0.73%. The diagram plots the displacement of the points of one free side of the yarn as shown in red dashed lines in Fig.11c

The Poisson ratio ν_{lt} introduced in Eq. (9) was determined by an inverse approach [44]. Simulations of the longitudinal compression tests with transverse expansion were performed and compared to the experiments (Fig. 13 and 14). The Poisson ratio was optimized so that the transverse expansion obtained by the simulation was as close as possible to the experiment (Fig. 14).

A priori, the Poisson ratio depends on the longitudinal compression strain and on the dimensions of the yarn. Fig. 15 shows the obtained Poisson ratio for longitudinal compression in the range 0.25% to 4%. Different lengths and widths of the specimen were considered. The obtained Poisson ratios of the fiber yarn varied with these factors. However, these variations were rather low. In a first approximation, for the sake of simplicity, a constant value of the Poisson ratio may be considered. For the binder yarn analyzed in the present work, the Poisson ratio was close to 11.8.

Fig. 16 compares the experimental transverse expansions with the corresponding simulations carried out with a Poisson ratio equal to 11.8. The comparison was carried out at different longitudinal compression strains. The transverse expansions obtained in the simulations and the experiments were in good agreement, in particular for moderate longitudinal compression strains.

In conclusion, a simple way to model transverse expansion is to consider a constant value of the Poisson ratio ν_{lt}. This proved correct for yarn dimensions similar to those in this study and moderate longitudinal compression strains (<5%). The obtained Poisson ratio (11.8) was much larger than classical values of more continuous materials ($\nu < 0.5$ for isotropic materials). This Poisson ratio reflected, at the meso scale, buckling of the fibers at the micro scale.

The binder yarns that were analyzed in this work were composed of parallel fibers without twist. The fibers could buckle easily thus giving a substantial transverse expansion. In the case of twisted yarns, this expansion should be less significant.

5. Mesoscopic simulations taking into account longitudinal compression and transverse expansion

5.1. Longitudinal compression of a warp yarn

A warp yarn of the unbalanced fabric shown in Fig. 4 was subjected to a longitudinal compression strain of 5%. The initial length specimen was 10 mm. In Fig. 17, the deformed shapes obtained by different simulation models were compared with the micro CT image of the deformed yarn segment. In Fig. 17b, the original model Eq. (7) was used. A global buckling of the yarn was obtained which did not correspond to the experiment. In Fig. 17c, the longitudinal compressive stiffness such as analyzed in section 3 was introduced in the simulation. There was no longer any buckling but the deformed shape suffered from a lack of transverse expansion. Finally, both longitudinal compressive stiffness and transverse expansion (as analyzed in section 4) were used in the simulation shown in Fig. 17d. The deformed shape obtained by the mesoscopic simulation was in good agreement with the experiment (Fig. 17d).

5.2. Compaction of a textile reinforcement

The unbalanced textile reinforcement presented in Fig. 4 and 6 was compacted between two Plexiglas plates ($\varepsilon_{compaction}$ = 44%). This simulation was carried out in section 2.2 with the original constitutive law Eq. (7) and led to spurious buckling of the binder yarn (Fig. 8). The simulation was now performed with the models proposed in section 3 and 4 for longitudinal compression and transverse expansion. The deformed shapes obtained by these simulations were compared to the experimental micro-CT images of the deformed fabric in Fig. 18. Buckling of the binder yarn was avoided when the longitudinal compression model presented in section 3 was taken into account (Fig. 18c). A correct transverse expansion was achieved when both longitudinal compression thickness and transverse expansion were modeled as proposed in sections 3 and 4 (Fig. 18d).

The compaction stress versus volume fraction is plotted Fig. 19 for three different mesh fineness. The number of nodes and wedge elements are specified in fig. 19. The compaction stresses obtained in the three case are very close. The coarse mesh is sufficient for this analysis. This is also the case for the other the calculations presented in the paper. A refinement of mesh used does not change the results significantly.

5.3. Compaction of a 3D textile reinforcement

A 3D orthogonal non-crimp woven fabric is presented in Fig. 20 in its undeformed state [48]. It was subjected to a global compaction between two Plexiglas plates ($\varepsilon_{compaction}$ = 22%). The yarns were made of glass fibers, and the principal properties of the 3D reinforcement are listed in Table 3. In addition to the warp and weft yarns that were in the plane of the fabric, Z-yarns insured the mechanical behavior of the reinforcement through its thickness.

The transverse compaction of the reinforcement was carried out within an X-ray tomograph. The deformed geometry obtained by micro-CT is presented Fig. 21a. The Z-yarns were subjected to longitudinal compression during the overall compaction of the reinforcement. Periodic boundary conditions are used for the Representative Unit Cell (RUC) [14, 43]. Two points of the boundary in so-called paired positions on two opposite boundaries have the same displacements. Fig. 21b shows the result of the simulation carried out with the initial constitutive law Eq. (7) in which the longitudinal tension and compression stiffnesses were the same. Consequently, the simulation led to spurious buckling of the Z-yarns. These wrinkles were avoided in the simulations shown in Fig. 21c by using the longitudinal compression law presented in section 3. The transverse expansion of the Z-yarns observed in the micro-CT image (Fig. 20a) was correctly obtained by the simulation in Fig. 21d when the transverse expansion model presented in section 4 was taken into account.

Conclusions

An analysis and a model of the longitudinal compression and transverse expansion of fiber yarns in meso FE simulations of textile composite reinforcements has been proposed. For certain loadings of a preform, some yarns can be subjected to longitudinal compression. This is particularly the case for binder yarns and z-yarns when the reinforcement is globally compacted, for instance before injection in an LCM process. The longitudinal compression must be taken into account in the mechanical model because it is specific and significantly different from the tensile behavior. The longitudinal compression stiffness is low in comparison to the tensile rigidity because the individual fibers buckle easily. Nevertheless it was shown for glass fiber yarns that this stiffness was fairly constant before the global buckling of the yarn.

The transverse expansion is substantial. The Poisson ratio expresses the buckling of individual fibers in the behavior of the yarn seen as a continuous material. It was shown in the present paper that

a constant Poisson ratio could be identified for glass fiber yarns (without twists) and that the value was substantial (11.8). Mesoscopic simulations taking into account longitudinal compression and transverse expansion gave results in good agreement with the experimental deformations obtained by micro-CT analysis. In a mesoscopic analysis, the yarn is seen as a continuous medium, which is a strong assumption, especially when the yarn is in longitudinal compression. The fibers buckle and lead to an important transverse expansion. The fibers are moving away from each other. The hypothesis of a continuous medium for the yarn, that supposes any mesoscopic analysis, is probably more questionable than for the yarns in tension. This point is a subject that will have to be investigated in future work concerning the mesoscopic analysis of textile reinforcements

The present experiments need to be performed on a large set of fiber yarns to check the validity of the results. In particular, it will be necessary to analyze to what extent and in what range a constant Poisson ratio can describe the transverse expansion. The influence of the internal structure of the yarn, and especially of the twists of the fibers, must be also investigated.

Acknowledgements

This work was supported by the ANR, (National Research Agency), grant aap-rmnp-2011-TAPAS and by the China Scholarship Council (CSC)(D. Wang).

References

[1] Lomov, S. V., Ivanov, D. S., Verpoest, I., Zako, M., Kurashiki, T., Nakai, H., & Hirosawa, S. (2007). Meso-FE modelling of textile composites: Road map, data flow and algorithms. Composites Science and Technology, 67(9), 1870-1891.

[2] Yu, W. R., Harrison, P., & Long, A. (2005). Finite element forming simulation for non-crimp fabrics using a non-orthogonal constitutive equation. Composites Part A: Applied Science and Manufacturing, 36(8), 1079-1093.

[3] Hamila, N., & Boisse, P. (2007). A meso–macro three node finite element for draping of textile composite preforms. Applied Composite Materials, 14(4), 235-250.

[4] Ten Thije, R. H. W., & Akkerman, R. (2009). A multi-layer triangular membrane finite element for the forming simulation of laminated composites. Composites Part A: Applied Science and Manufacturing, 40(6), 739-753.

[5] Gereke, T., Döbrich, O., Hübner, M., & Cherif, C. (2013). Experimental and computational composite textile reinforcement forming: a review. Composites Part A: Applied Science and Manufacturing, 46, 1-10.

[6] Wang, P., Legrand, X., Boisse, P., Hamila, N., & Soulat, D. (2015). Experimental and numerical analyses of manufacturing process of a composite square box part: Comparison between textile reinforcement forming and surface 3D weaving. Composites Part B: Engineering, 78, 26-34.

[7] Dangora, L. M., Mitchell, C., White, K. D., Sherwood, J. A., & Parker, J. C. (2016). Characterization of temperature-dependent tensile and flexural rigidities of a cross-ply thermoplastic lamina with implementation into a forming model. International Journal of Material Forming, 1-10. DOI 10.1007/s12289-016-1327-2

[8] Advani, S. G. (Ed.). (1994). Flow and rheology in polymer composites manufacturing (No. 10). Elsevier science.

[9] Ruiz, E., Achim, V., Soukane, S., Trochu, F., & Bréard, J. (2006). Optimization of injection flow rate to minimize micro/macro-voids formation in resin transfer molded composites. Composites science and technology, 66(3), 475-486.
[10] Durville, D. (2010). Simulation of the mechanical behaviour of woven fabrics at the scale of fibers. International journal of material forming, 3(2), 1241-1251.
[11] Latil, P., Orgéas, L., Geindreau, C., Dumont, P. J. J., & Du Roscoat, S. R. (2011). Towards the 3D in situ characterisation of deformation micro-mechanisms within a compressed bundle of fibres. Composites Science and Technology, 71(4), 480-488.
[12] El Said, B., Ivanov, D., Long, A. C., & Hallett, S. R. (2016). Multi-scale modelling of strongly heterogeneous 3D composite structures using spatial Voronoi tessellation. Journal of the Mechanics and Physics of Solids, 88, 50-71.
[13] Daelemans, L., Faes, J., Allaoui, S., Hivet, G., Dierick, M., Van Hoorebeke, L., & Van Paepegem, W. (2016). Finite element simulation of the woven geometry and mechanical behaviour of a 3D woven dry fabric under tensile and shear loading using the digital element method. Composites Science and Tech., 137, 177-187.
[14] Miehe, C., & Dettmar, J. (2004). A framework for micro–macro transitions in periodic particle aggregates of granular materials. Computer Methods in Applied Mechanics and Engineering, 193(3), 225-256.
[15] Tang, X., & Whitcomb, J. D. (2003). General techniques for exploiting periodicity and symmetries in micromechanics analysis of textile composites. Journal of Composite Materials, 37(13), 1167-1189.
[16] Wan, Y., Zhang, F., Gu, B., Sun, B., & Wang, Y. (2015). Predicting dynamic in-plane compressive properties of multi-axial multi-layer warp-knitted composites with a meso-model. Composites Part B: Engineering, 77, 278-290.
[17] Rahali, Y., Giorgio, I., Ganghoffer, J. F., & Dell'Isola, F. (2015). Homogenization à la Piola produces second gradient continuum models for linear pantographic lattices. International Journal of Engineering Science, 97, 148-172.
[18] Giannaros, E., Kotzakolios, T., Tsantzalis, S., & Kostopoulos, V. (2017). Implementation and calibration of meso-scale modeling technique for simulation of tensile behavior of fabric materials. Composites Part B: Engineering, 119, 1-9.
[19] Pickett, A. K., & Fouinneteau, M. R. C. (2006). Material characterisation and calibration of a meso-mechanical damage model for braid reinforced composites. Composites Part A: Applied Science and Manufacturing, 37(2), 368-377.
[20] Xu, J., Lomov, S. V., Verpoest, I., Daggumati, S., Van Paepegem, W., & Degrieck, J. (2016). A comparative study of twill weave reinforced composites under tension–tension fatigue loading: Experiments and meso-modelling. Composite Structures, 135, 306-315.
[21] Raman, V., Drissi-Habti, M., Guillaumat, L., & Khadhour, A. (2016). Numerical simulation analysis as a tool to identify areas of weakness in a turbine wind-blade and solutions for their reinforcement. Composites Part B: Engineering, 103, 23-39.
[22] Badel, P., Vidal-Sallé, E., Maire, E., & Boisse, P. (2008). Simulation and tomography analysis of textile composite reinforcement deformation at the mesoscopic scale. Composites Science and Technology, 68(12), 2433-2440.
[23] Bayraktar, H., Ehrlich, D., Scarat, G., McClain, M., Timoshchuk, N., & Redman, C. (2015). Forming and performance analysis of a 3D-woven composite curved beam using meso-scale FEA. Sampe Journal, 51(3), 23-29.
[24] Bickerton, S., Šimáček, P., Guglielmi, S. E., & Advani, S. G. (1997). Investigation of draping and its effects on the mold filling process during manufacturing of a compound curved composite part. Composites Part A: Applied Science and Manufacturing, 28(9), 801-816.
[25] Tran, T., Comas-Cardona, S., Abriak, N. E., & Binetruy, C. (2010). Unified microporomechanical approach for mechanical behavior and permeability of misaligned unidirectional fiber reinforcement. Composites Science and Technology, 70(9), 1410-1418.
[26] Causse, P., Ruiz, E., & Trochu, F. (2013). Influence of preforming on the quality of curved composite parts manufactured by flexible injection. International journal of material forming, 6(3), 341-362.
[27] Zeng, X., Brown, L. P., Endruweit, A., Matveev, M., & Long, A. C. (2014). Geometrical modelling of 3D woven reinforcements for polymer composites: Prediction of fabric permeability and composite mechanical properties. Composites Part A: Applied Science and Manufacturing, 56, 150-160.
[28] Blais, M., Moulin, N., Liotier, P. J., & Drapier, S. (2017). Resin infusion-based processes simulation: coupled Stokes-Darcy flows in orthotropic preforms undergoing finite strain. International Journal of Material Forming, 10(1), 43-54.
[29] Caglar, B., Orgéas, L., du Roscoat, S. R., Sozer, E. M., & Michaud, V. (2017). Permeability of textile fabrics with spherical inclusions. Composites Part A: Applied Science and Manufacturing, 99, 1-14.
[30] Sadykova, F. K. (1972). The Poisson ratio of textile fibres and yarns. Fibre Chemistry, 3(2), 180-183.

[31] Ravirala, N., Alderson, K. L., Davies, P. J., Simkins, V. R., & Alderson, A. (2006). Negative Poisson's ratio polyester fibers. Textile research journal, 76(7), 540-546.
[32] Du, Z., Zhou, M., Liu, H., & He, L. (2015). Study on negative Poisson's ratio of auxetic yarn under tension: Part 1–Theoretical analysis. Textile Research Journal, 85(5), 487-498.
[33] Du, Z., Zhou, M., He, L., & Liu, H. (2015). Study on negative Poisson's ratio of auxetic yarn under tension: Part 2–Experimental verification. Textile Research Journal, 85(7), 768-774.
[34] Takatera, M., Arichi, T., Peiffer, J., Zhu, C., & Kim, K. (2017). Continuous measurement of apparent Poisson's ratio for yarn based on omni-directional diameters. Textile Research Journal, 87(6), 739-746.
[35] Xiao, H., Bruhns, O. T., & Meyers, A. (1997). Hypo-elasticity model based upon the logarithmic stress rate. Journal of Elasticity, 47(1), 51-68.
[36] De Borst R., Crisfield, M. A., Remmers, J. J., & Verhoosel, C. V. (2012). Nonlinear finite element analysis of solids and structures. John Wiley & Sons.
[37] T. Belytschko, W. K. Liu, B. Moran, and K. Elkhodary, (2013) Nonlinear Finite Elements for Continua and Structures. John wiley & sons.
[38] Naghdi, P. M., & Wainwright, W. L. (1961). On the time derivative of tensors in mechanics of continua. Quarterly of Applied Mathematics, 19(2), 95-109.
[39] Green, A. E., & Naghdi, P. M. (1965). A general theory of an elastic-plastic continuum. Archive for rational mechanics and analysis, 18(4), 251-281.
[40] Jaumann, G. (1911). Geschlossenes System physikalischer und chemischer Differentialgesetze. Sitzungsber. Akad. der Wissenschaften in Wien, CXVII (Mathematisch IIa), 120, 385-530
[41] Johnson, G. C., & Bammann, D. J. (1984). A discussion of stress rates in finite deformation problems. International Journal of Solids and Structures, 20(8), 725-737.
[42] Boisse, P., Gasser, A., Hagege, B., & Billoet, J. L. (2005). Analysis of the mechanical behavior of woven fibrous material using virtual tests at the unit cell level. Journal of materials science, 40(22), 5955-5962.
[43] Badel, P., Vidal-Sallé, E., & Boisse, P. (2008). Large deformation analysis of fibrous materials using rate constitutive equations. Computers & Structures, 86(11), 1164-1175.
[44] Hughes, T. J., & Winget, J. (1980). Finite rotation effects in numerical integration of rate constitutive equations arising in large-deformation analysis. International journal for numerical methods in engineering, 15(12), 1862-1867.
[45] Komeili, M., & Milani, A. S. (2016). On effect of shear-tension coupling in forming simulation of woven fabric reinforcements. Composites Part B: Engineering, 99, 17-29.
[46] Schnur, D. S., & Zabaras, N. (1992). An inverse method for determining elastic material properties and a material interface. International Journal for Numerical Methods in Engineering, 33(10), 2039-2057.
[47] Naouar, N., Vidal-Sallé, E., Schneider, J., Maire, E., & Boisse, P. (2014). Meso-scale FE analyses of textile composite reinforcement deformation based on X-ray computed tomography. Composite Structures, 116, 165-176.
[48] Naouar, N., Vidal-Salle, E., Schneider, J., Maire, E., & Boisse, P. (2015). 3D composite reinforcement meso FE analyses based on X-ray computed tomography. Composite Structures, 132, 1094-1104.
[49] Boussu, F., Cristian, I., & Nauman, S. (2015). General definition of 3D warp interlock fabric architecture. Composites Part B: Engineering, 81, 171-188.

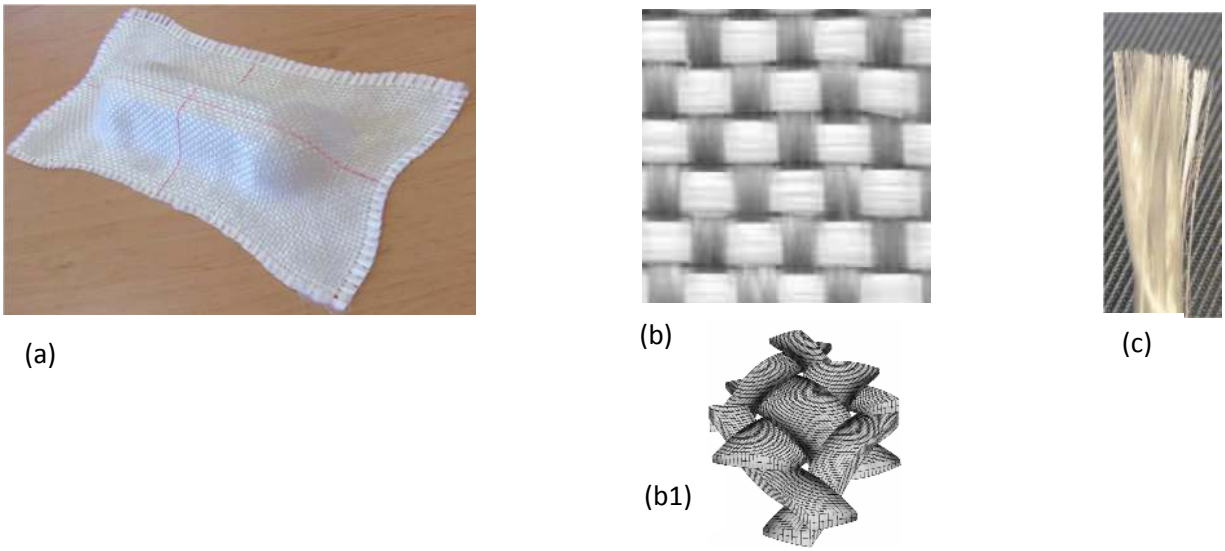

Figure 1. The three scales of the fiber reinforcement.
(a) Macroscopic scale, (b) mesoscopic scale, (b1) mesoscale FE analysis, (c) microscopic scale.

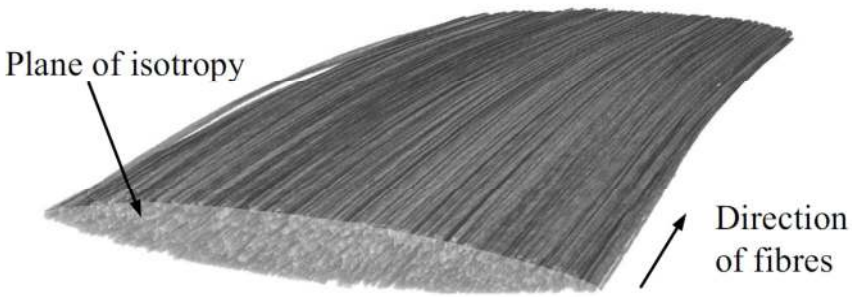

Figure 2. Yarn in a textile reinforcement. X-ray tomography imaging.

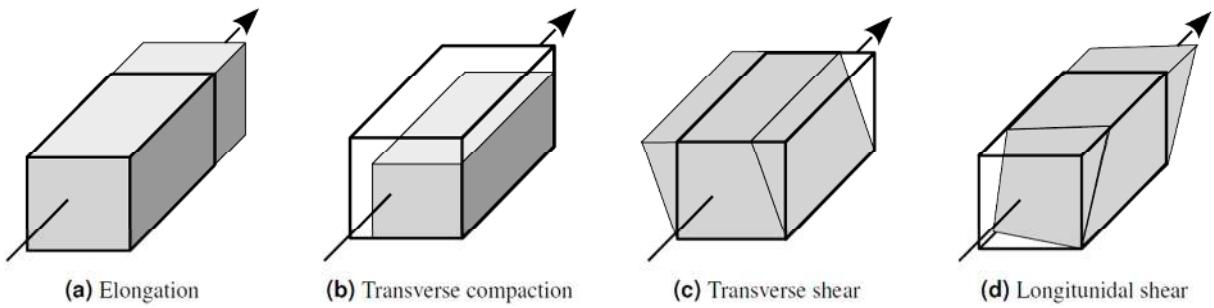

Figure 3. Different deformation modes of the yarn at mesoscopic scale.

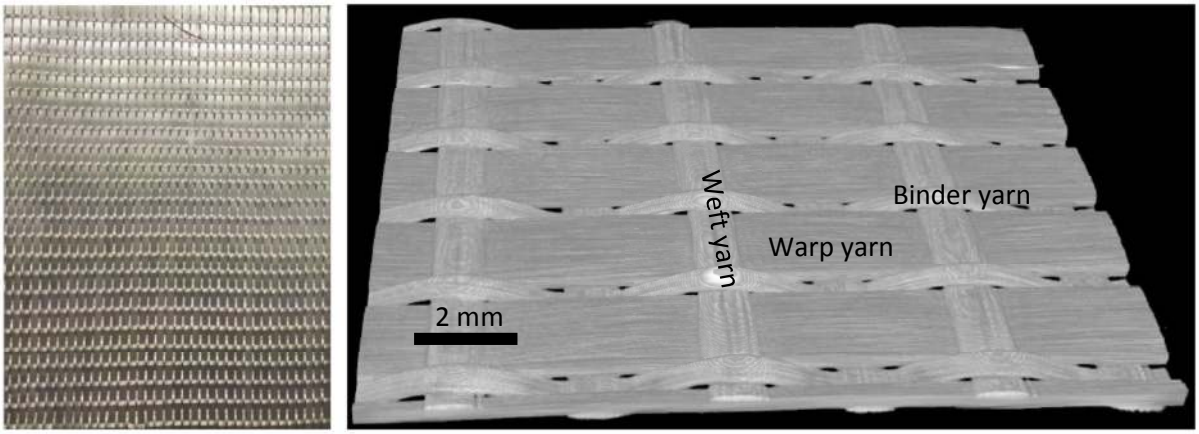

Figure 4. Unbalanced textile reinforcement

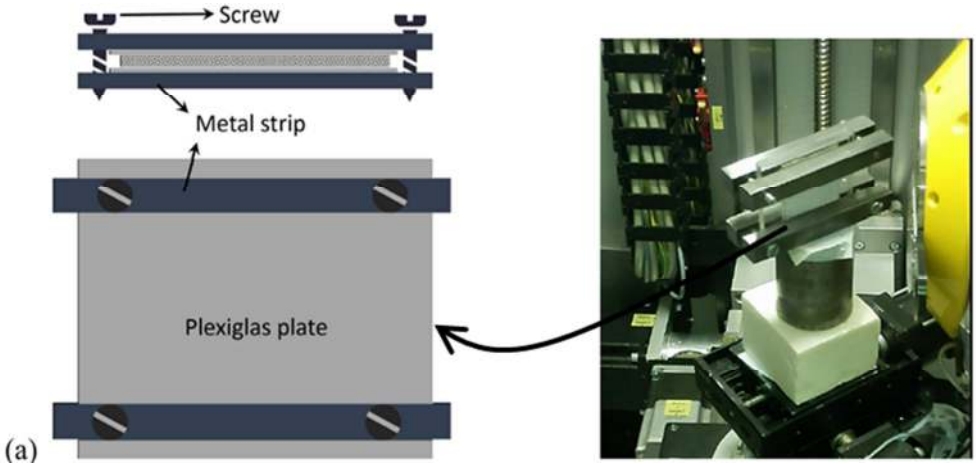

Figure 5. Transverse compaction of the textile reinforcement between two plates within a X-ray computed tomography system

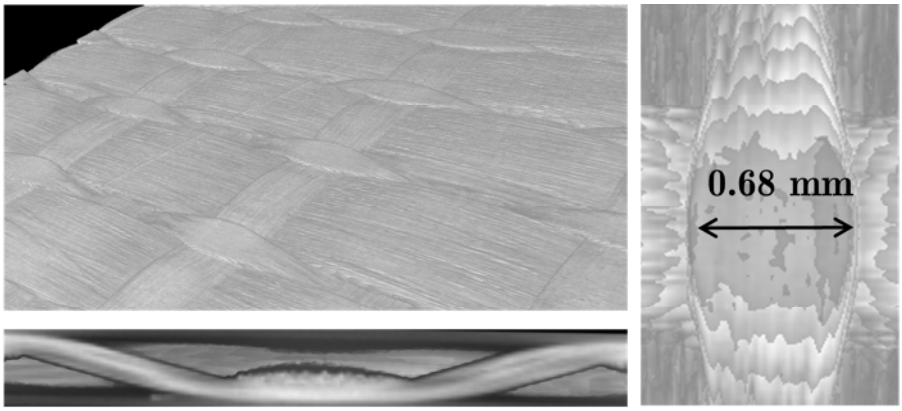

Figure 6. Deformed geometry of the yarns of the fabric after compaction

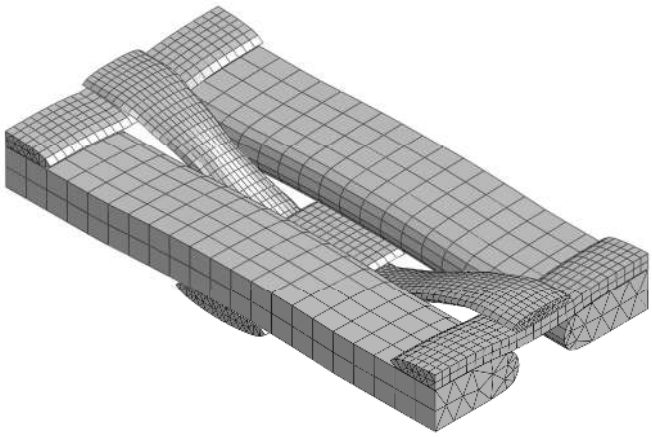

Figure 7. Meso FE mesh of the RUC ((Representative Unit Cell)

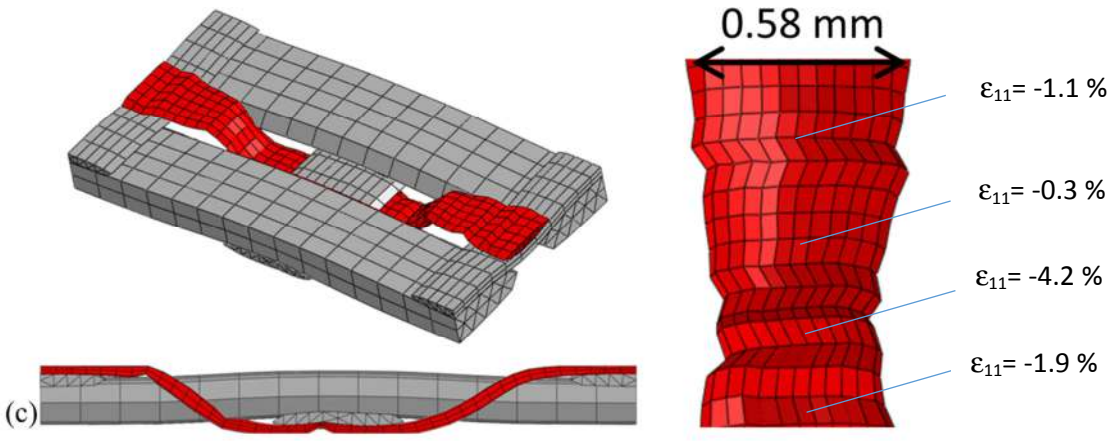

Figure 8. Simulation of the compaction based on the initial mechanical model presented in section 2. ε_{11} is the strain in the fiber direction.

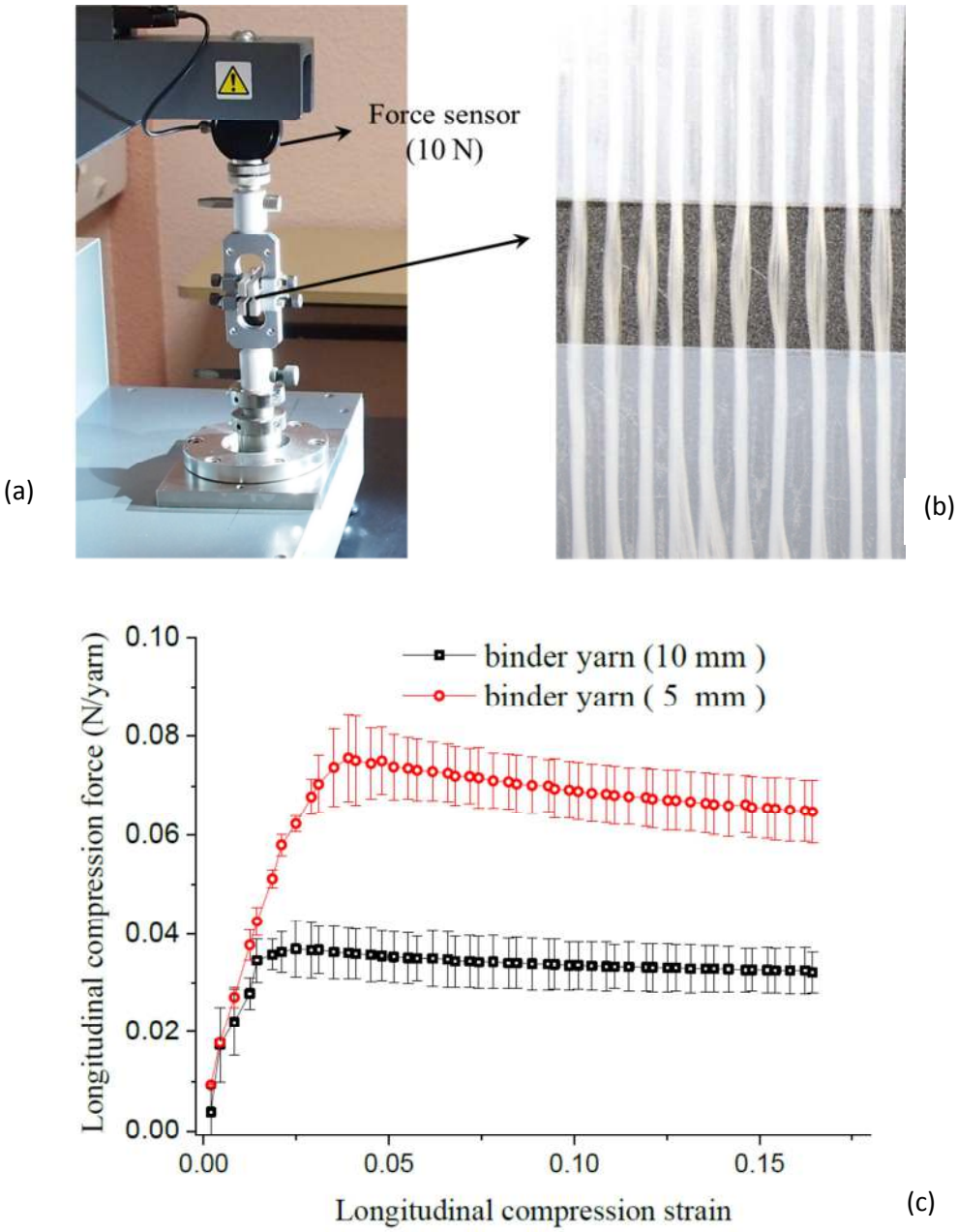

Figure 9. Longitudinal compression experiments on binder yarns
(a) Experimental setup. (b) Tested specimens.
(c) Longitudinal compression curves for two different length of the specimens

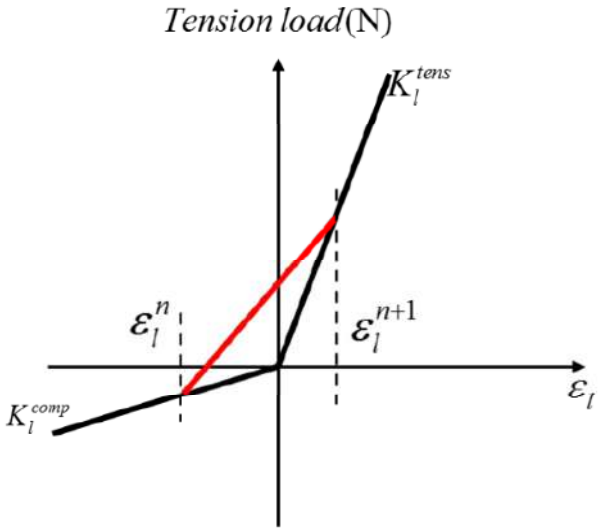

Figure 10. Transition between longitudinal tension and compression

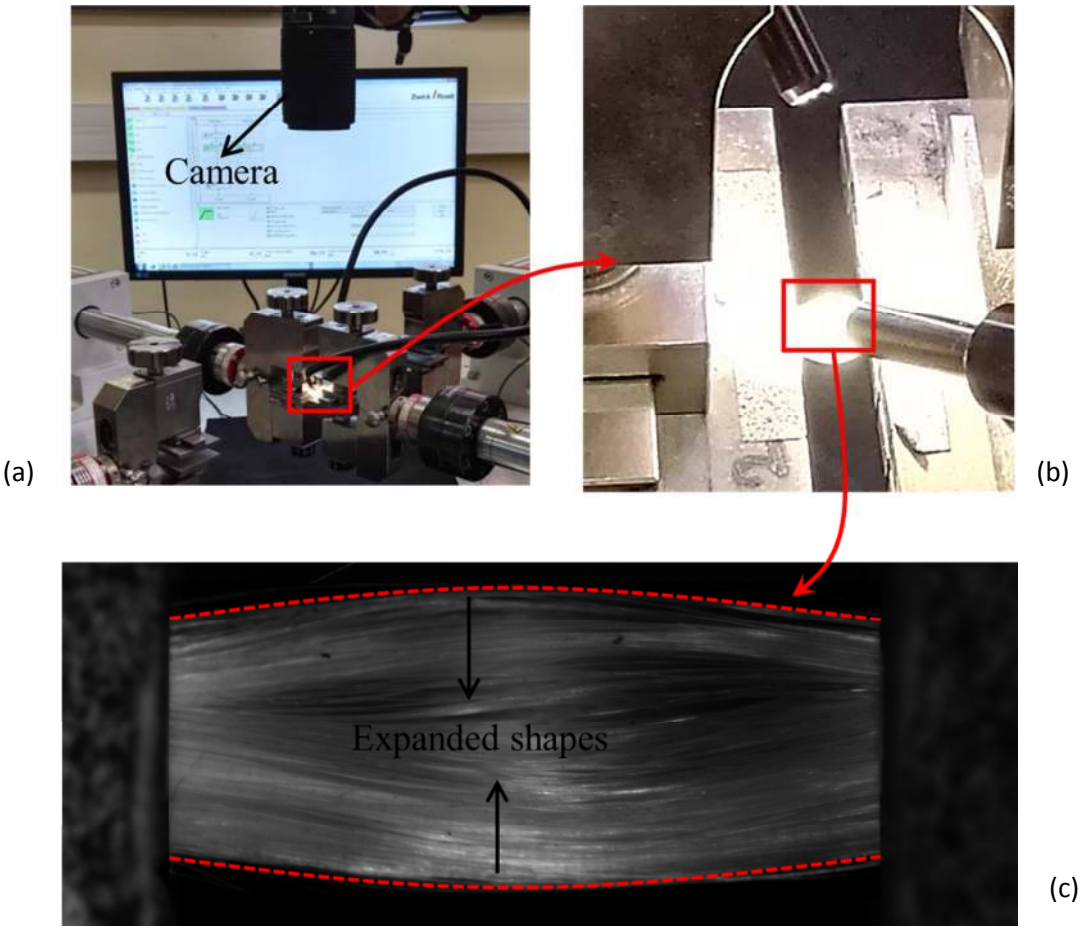

Figure 11. Transverse expansion experiment: (a)(b) experimental setup,

(c) transverse expansion of the yarn in longitudinal compression

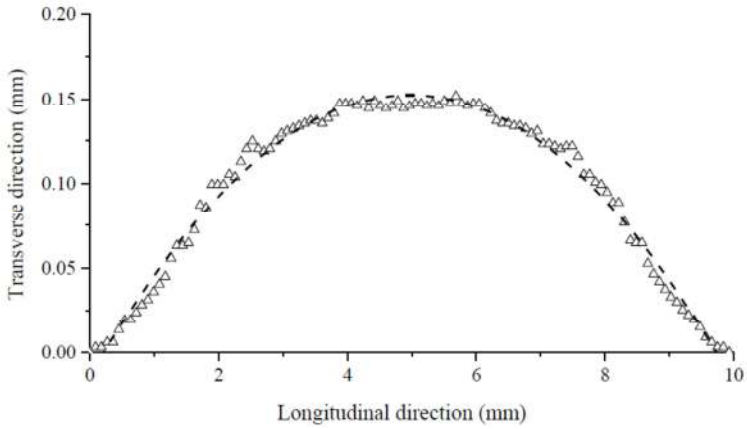

Fig. 12. Transverse expansion along a 10 mm yarn for a 0.73% longitudinal compression.

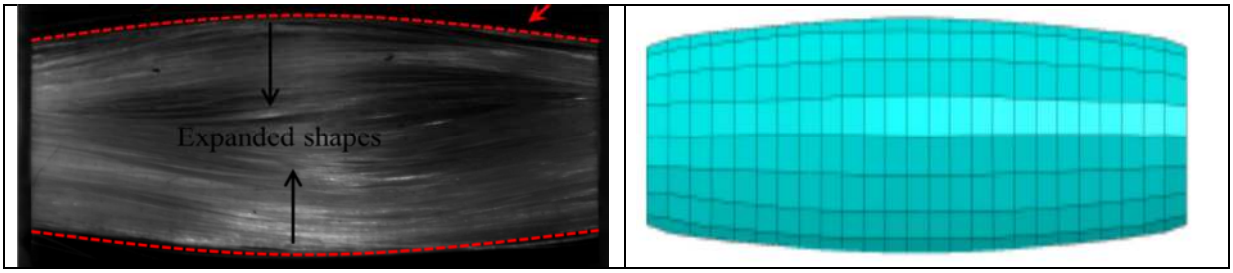

Figure 13. Inverse approach to determine the Poisson ratio in longitudinal compression.
(a) Experiments, (b) Simulation.

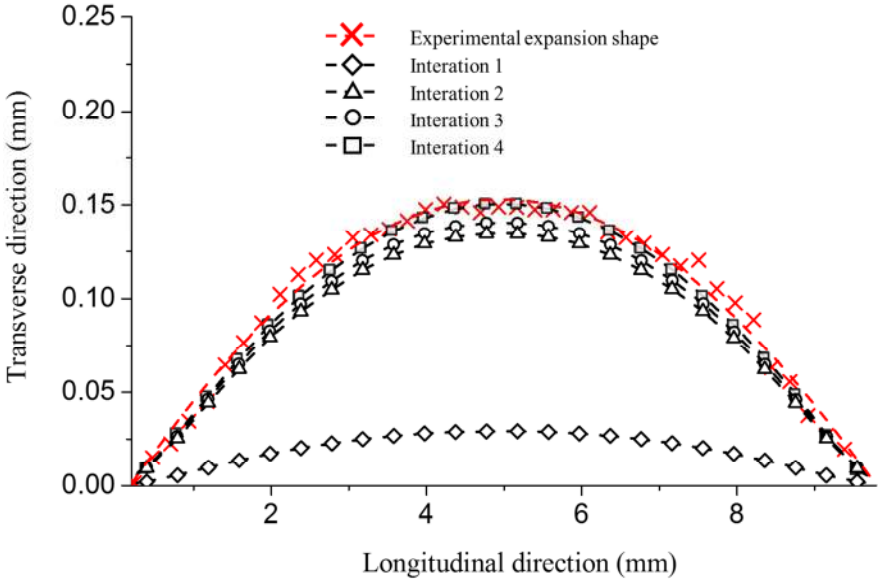

Figure 14. Determination of the Poisson ratio by inverse fitting

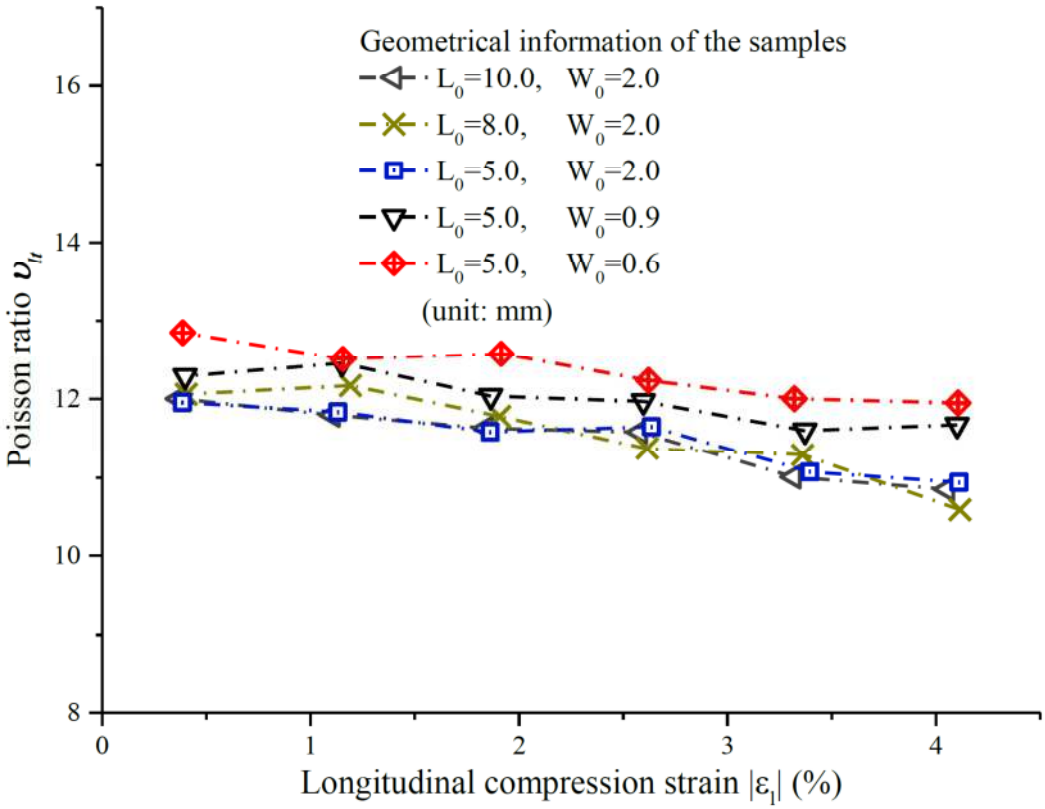

Figure 15. Measured Poisson Ratios for different dimensions and longitudinal compression strains (L_0 : initial length; W_0 initial width)

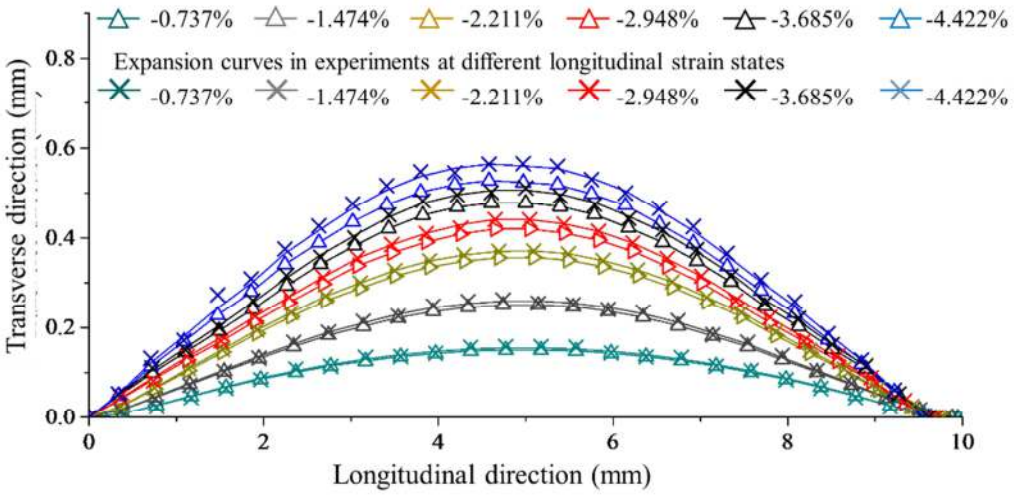

Fig. 16. Comparison of experimental and simulated transverse expansion for ν_{lt}=11.8 at different longitudinal compression strains

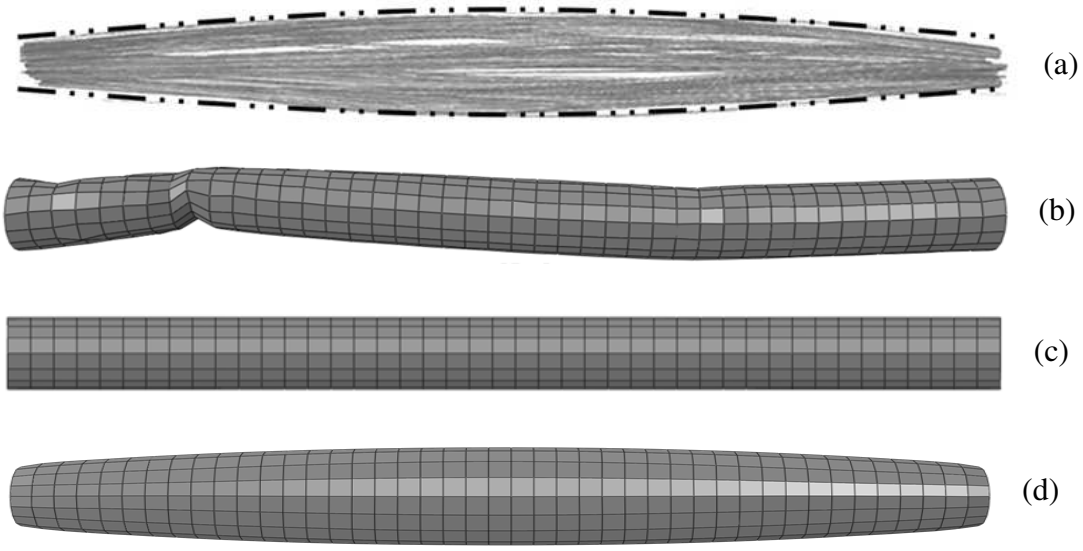

Figure 17. Longitudinal compression of a warp yarn.

(a) Micro CT image of the deformed shape. (b) Simulation with the initial model.

(c) Simulation taking longitudinal compression stiffness (d) Simulation taking longitudinal compression stiffness and transverse expansion.

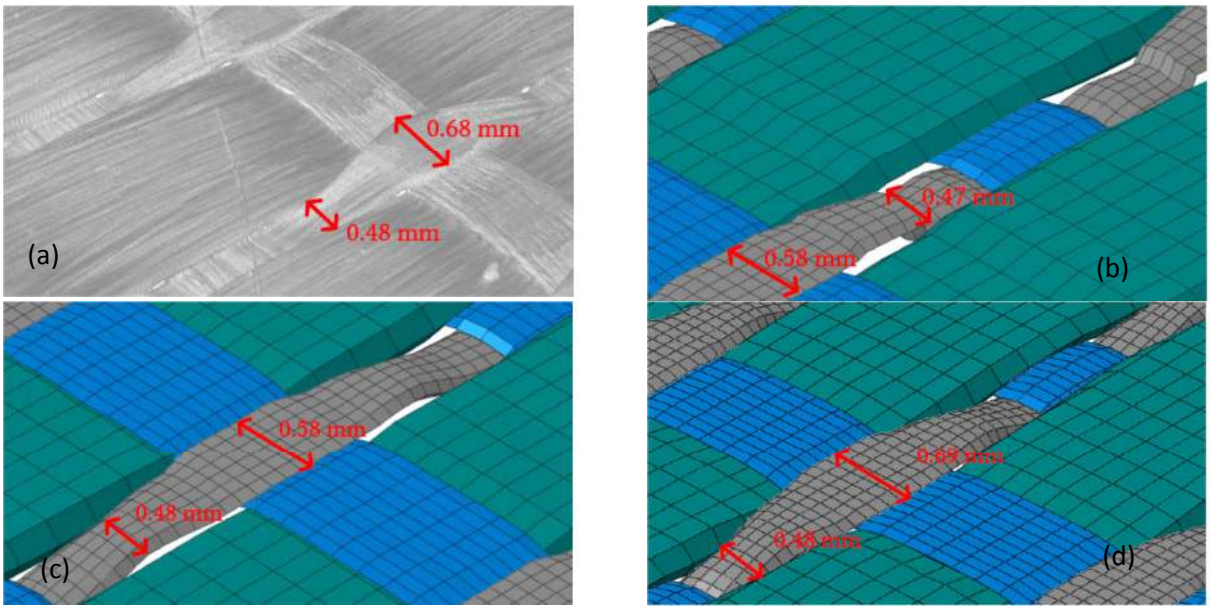

Figure 18. Transverse compaction of an unbalanced textile reinforcement.

(a) Micro-CT analysis (b) Simulation with the original model.

(c) Simulation taking into account the model of the longitudinal compression presented section 3.

(d) Simulation taking into account the model of the longitudinal compression presented section 3 and the model of the transverse expansion presented section 4.

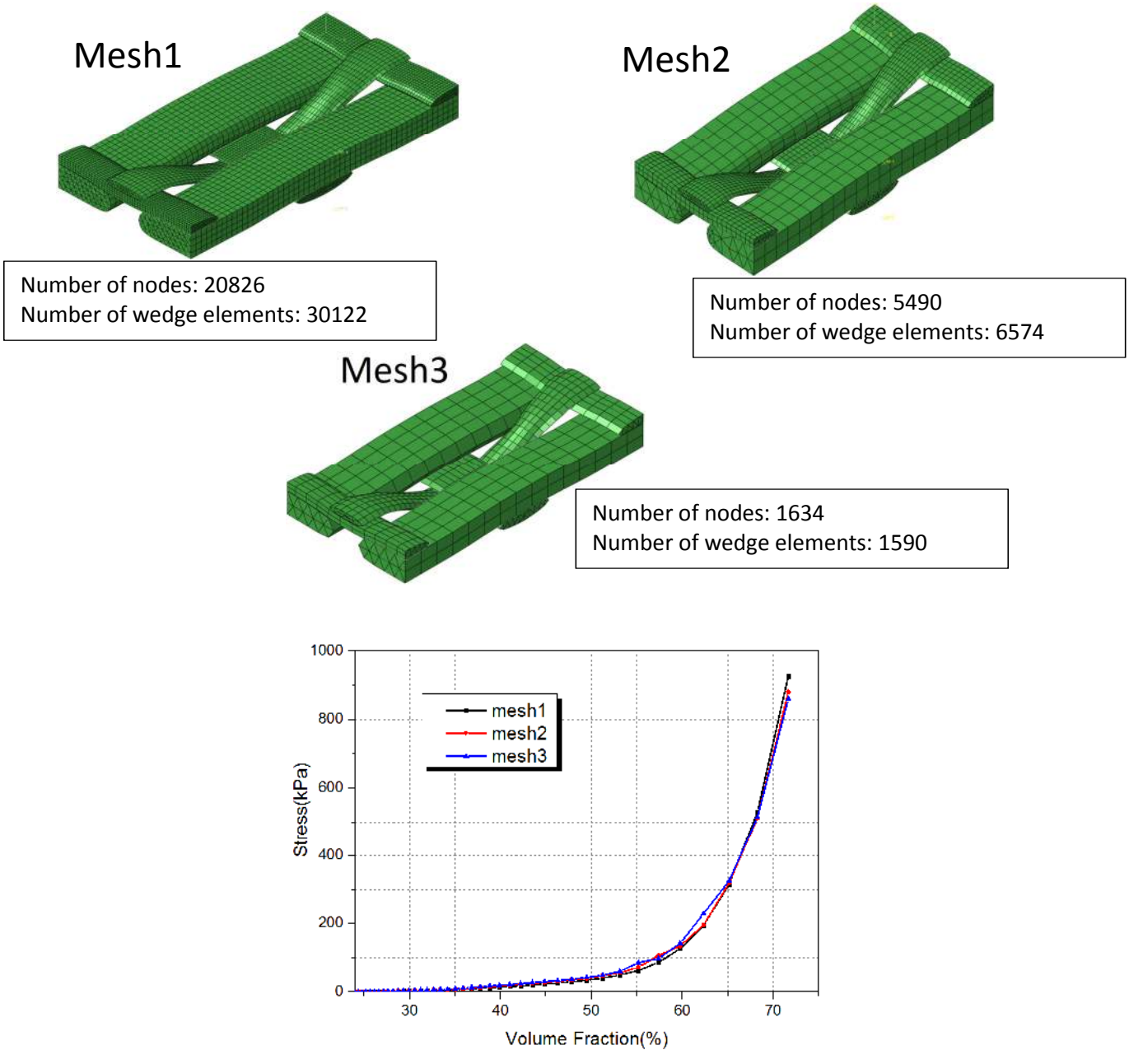

Figure 19. Compaction stress versus volume fraction in the transverse compaction of an unbalanced textile reinforcement for three different meshes.

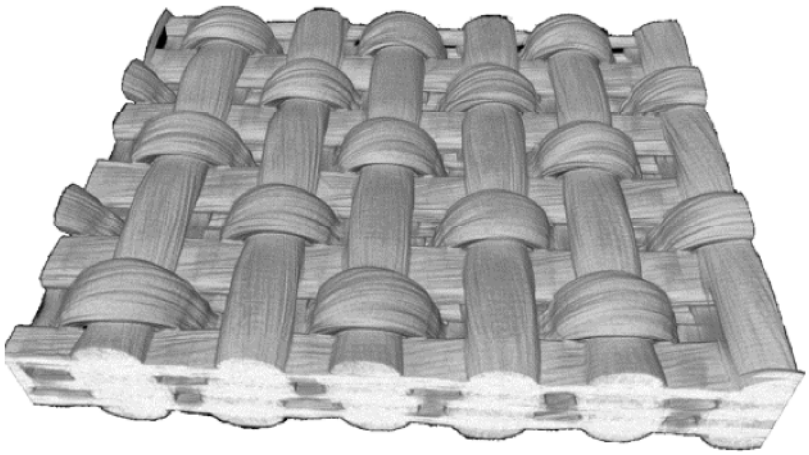

Figure 20. 3D orthogonal non-crimp woven fabric. Initial state

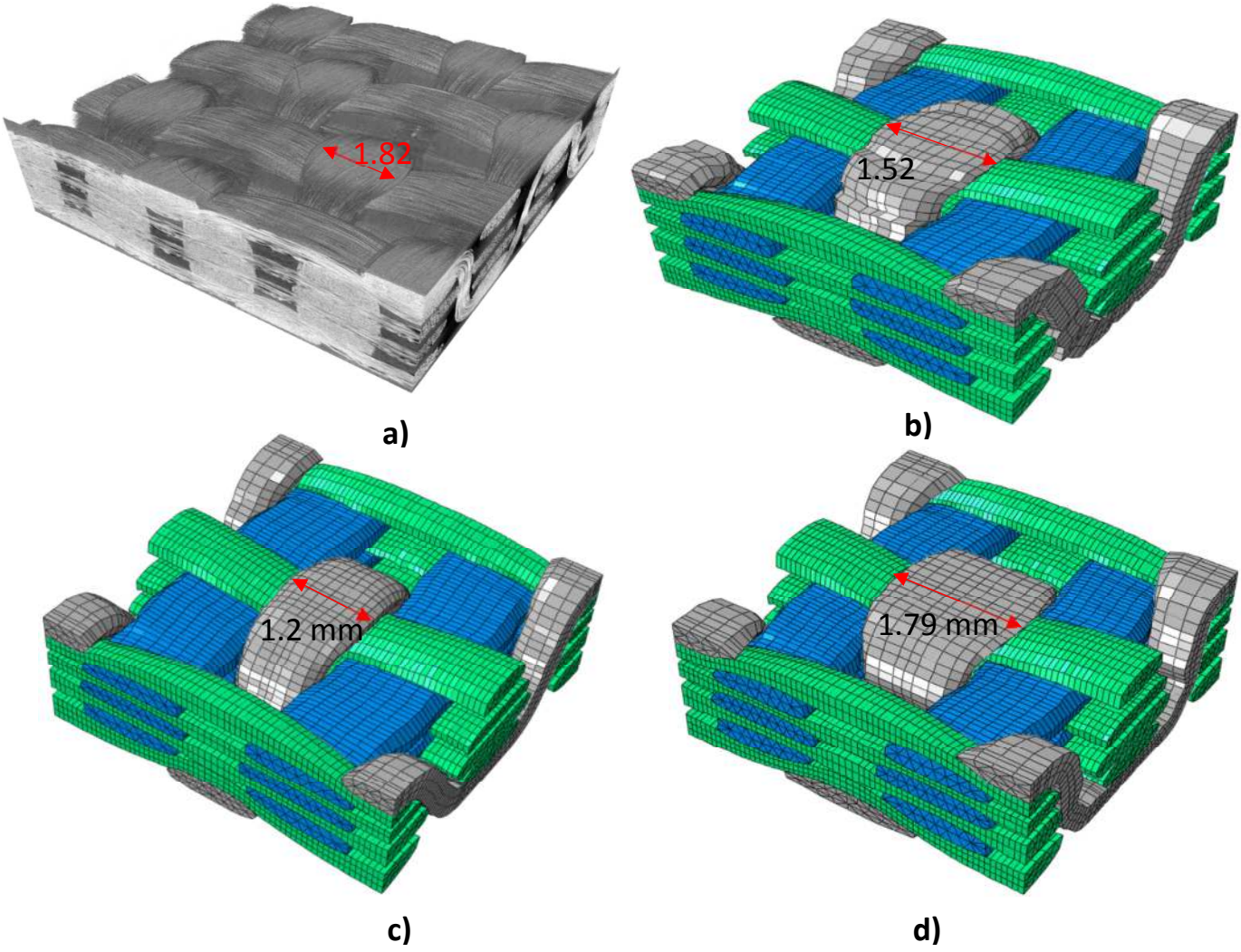

Figure 21. Compaction of a 3D reinforcement. Comparison of the deformed shapes.
(a) X-ray tomography (b) original mesoscopic model
(c) with longitudinal compression model of section 3 (d) with longitudinal compression model of section 3 and transverse expansion model of section 4.

A_0	B_0	n	p
$0.02MPa$	$0.015MPa$	1000	20.6
$(K_l)_{warp}$	$(K_l)_{weft}$	$(K_l)_{binder}$	G_{lt}
$19000\,N$	$2740\,N$	$2340\,N$	$20\,MPa$

Table 1. Mechanical parameters of the unbalanced fabric, K_l is the tensile stiffness of the yarn (Tension load/extension strain), G_{lt} is the Coulomb modulus.

Thickness	*Material density*	*Area density*
$0.72\,mm$	$0.522\,kg/m^3$	$2204\,kg/m^2$

	Warp	*Binder*	*Weft*
Sectional area	*0.5735 mm2*	*0.0798 mm2*	*0.0868 mm2*
Insertion density	*4 yarns per centimeter*	*4 yarns per centimeter*	*4 yarns per centimeter*

Table 2. Characteristics of the unbalanced fabric

Roving *Tex (g/km), ±6%*	*Filament* diameter (μm)	*Number of filaments in a yarn*	*Area* density *(g/m2)*	Fabric thickness *(mm)*
900	15	2000	2722	3.1

	Warp	*Binder*	*Weft*
Sectional area	*0.6 mm2*	*0.52 mm2*	*0.53 mm2*
Insertion density	*4 yarns per centimeter*	*4 yarns per centimeter*	*4 yarns per centimeter*

Table 3. Characteristics of the non-crimp 3D orthogonal weave reinforcement